Chapter 1

Introduction

1.1 Kinetics of phase transition

The primary focus of this thesis is on the fundamental study of phase segregation kinetics in polymeric fluids. Soft materials have very simple structures of their components but can be arranged in very complicated ways, forming very interesting morphologies with significant applications across various fields [2,3]. A standout characteristic of soft materials is their inherent ability to undergo self-assembly [2–5]. Soft materials demonstrate the remarkable capability to autonomously self-assemble, generating highly intricate structures without needing external assistance [2,3]. Comprehending self-assembly requires understanding the kinetics of phase transition, which involves phenomena such as spinodal decomposition, nucleation, and domain evolution [1,3,6]. Two types of structures emerge in varying scenarios: those formed under equilibrium conditions and those arising in non-equilibrium situations. At equilibrium, soft matter can form various complex and exciting phases [2,3]. Under non-equilibrium conditions, phase transitions give rise to the emergence of self-assembled structures [2,3]. Depending on external parameters like temperature (T) and pressure (P), many systems have multiple phases with different behaviors. We can also observe that quantitative parameter changes lead to qualitative structure alterations. This phenomenon of non-equilibrium evolution is called as the kinetics of phase transition or domain evolution. We are interested in the non-equilibrium systems in which parameters are drastically changed. These systems can be categorized into two primary classes: those that reach a steady state through external driving forces and those that relax in an equilibrium state without external assistance. First, let's define out-of-equilibrium, or non-equilibrium, or far-from-equilibrium systems. These systems are characterized by two critical factors: (1) the presence of time-dependent macroscopic variables, such as temperature or pressure, or (2) the existence of macroscopic currents of fundamental quantities like mass, heat, or charge.

The theory of domain coarsening has been a subject of intensive study for many decades, beginning with pioneering work by Lifshitz [7,8], Lifshitz and Slyozov [9], and Wagner [10]. During the time interval, several outstanding reviews have been published on the same subject, showcasing notable contributions from Binder [11], Furukawa [12], and Langer [13]. Many recent works have enhanced our understanding of such problems, particularly pure and isotropic systems [14–18]. The scope of challenges in this field extends from exploring clustering dynamics in the early universe to understanding the growth of nanostructures. Advancements in theoretical and experimental backgrounds of phase ordering kinetics are made for various systems such as ferromagnets, antiferromagnets, liquid crystals, and liquid helium.

Let's take an elementary example in this context, i.e., the transition from a paramagnetic to a ferromagnetic state. We consider the sudden change in the temperature of the system referred to as a temperature quench under zero external magnetic field ($h = 0$). The phase diagram is shown in Fig.1.1 [1]. For $T > T_c$, the system resides in paramagnetic state. However, following the quench to temperatures below T_c, the system prefers a magnetized state, where spins tend to align either upwards or downwards. Quenching the temperature drives the system into an unstable, disordered state. As time progresses, the system exhibits the emergence and growth of spin regions of approximately equal size in both up and down directions.

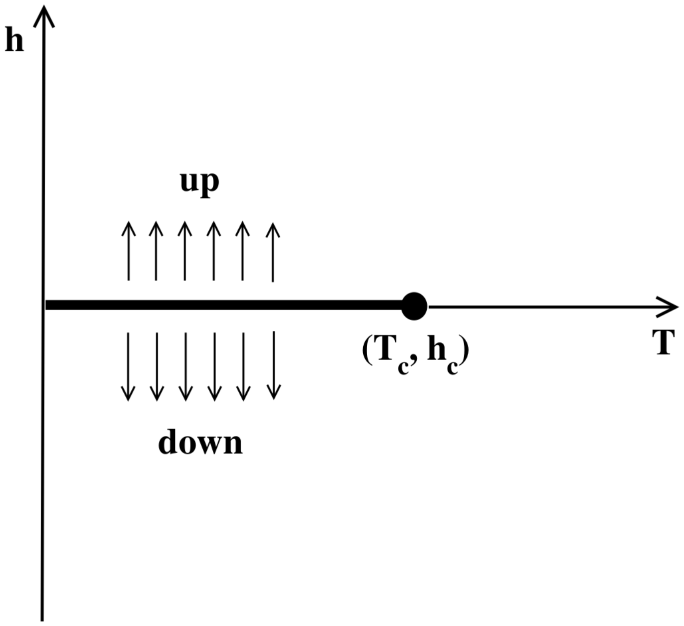

Fig. 1.1: Phase diagram for ferromagnet [1]. Here T and h represents the temperature and the magnetic field, respectively. The line $(T < T_c, h = 0)$ denotes the first-order transition, and the point $(T_c, h_c = 0)$ signifies the second-order critical point. When $T > T_c$, the system is in a disordered state, whereas for $T < T_c$, it falls in magnetized state with spins aligned either upwards or downwards.

1.1.1 Liquid-liquid unmixing

Now, consider the example of the phase segregation in two liquids that are miscible at high temperatures. Still, as we lower the temperature of the system, they separate into distinct phases. Using this example, we will introduce a statistical model that can help to calculate the system's equilibrium state as a function of temperature and composition. Our primary objective is to compute the free energy of mixing [3,19]. Let's consider two liquids, denoted as A and B, in an unmixed state, characterized by the combined free energies $F_A + F_B$. Following mixing, the combined free energy becomes F_{A+B}. The free energy of mixing, denoted as F_{mix}, is calculated as $F_{mix} = F_{A+B} - (F_A + F_B)$. Since $F = U - TS$, we need to evaluate the entropy and free energy changes upon mixing.

We have taken the volume of species A to be V_A and species B to be V_B, and there is no change in volume on mixing. We consider the composition of the system in terms of volume fraction ϕ defined as $\phi_A = V_A/(V_A + V_B)$, and $\phi_B = V_B/(V_A + V_B)$. To simplify, we assume that the volume of both types of molecules is the same. Here, we utilize the Boltzmann formula to compute entropy, expressed as $S = -k_B \sum_i \rho_i \ln \rho_i$. Here, ρ_i is the probability of finding the particle in state i. In our system, each site can be occupied by either A or B-type molecules, with probabilities of finding these molecules denoted as ϕ_A and ϕ_B, respectively. Therefore, the entropy upon mixing is expressed as:

$$S_{mix} = -k_B(\phi_A \ln \phi_A + \phi_B \ln \phi_B). \tag{1.1}$$

Here, the mean-field assumption is taken that the neighboring sites are independent of each other. Now, we calculate the energy of mixing U_{mix}. We assume that molecules interact only with their nearest neighbors, and these interactions are pairwise additive. We consider that the interaction energy between two neighboring A-type molecules is denoted as ϵ_{AA}, between two neighboring B-type molecules as ϵ_{BB}, and between neighboring A and B-type molecules as ϵ_{AB}. We apply the mean-field assumption, where a given site has an average of $z\phi_A$ and $z\phi_B$ number of A and B-type neighbors, regardless of whether A or B-type molecules occupy the site itself. Here, z is the coordination number of the lattice. Using this assumption, we can write the expression for interaction energy per site as $(z/2)({\phi_A}^2\epsilon_{AA} + {\phi_B}^2\epsilon_{BB} + 2\phi_A\phi_B\epsilon_{AB})$. In the case of an unmixed state, the interaction energy can be written as $(z/2)(\phi_A\epsilon_{AA} + \phi_B\epsilon_{BB})$. Thus the energy of mixing can be determined as the difference between the energy after and before mixing:

$$U_{mix} = \frac{z}{2}[({\phi_A}^2 - \phi_A)\epsilon_{AA} + ({\phi_B}^2 - \phi_B)\epsilon_{BB} + 2\phi_A\phi_B\epsilon_{AB}]. \tag{1.2}$$

We assume the incompressible mixture, therefore, $\phi_A + \phi_B = 1$. The expression for energy of mixing in Eq. 1.2 can be written in terms of $\phi_A = \phi = 1 - \phi_B$, as follows [3,19]:

$$\begin{aligned} U_{mix} &= \frac{z}{2}[(\phi^2 - \phi)\epsilon_{AA} + ((1-\phi)^2 - (1-\phi))\epsilon_{BB} + 2\phi(1-\phi)\epsilon_{AB}], \\ &= \frac{z}{2}\phi(1-\phi)[2\epsilon_{AB} - \epsilon_{AA} - \epsilon_{BB}]. \end{aligned} \tag{1.3}$$

To characterize the energetic interaction between molecules Flory-Huggins interaction, we introduce a dimensionless parameter χ defined as [3,19]:

$$\chi = \frac{z}{2k_BT}\phi(1-\phi)[2\epsilon_{AB} - \epsilon_{AA} - \epsilon_{BB}]. \tag{1.4}$$

Therefore,

$$U_{mix} = \chi\phi(1-\phi)k_BT = \chi\phi_A\phi_Bk_BT. \tag{1.5}$$

Now, we can write the free energy $F = U - TS$ of the system as:

$$\frac{F_{mix}}{k_BT} = \phi_A \ln\phi_A + \phi_B \ln\phi_B + \chi\phi_A\phi_B. \tag{1.6}$$

The first term of Eq. 1.6 originates from entropy, which encourages mixing, and the second term arises from energetic considerations and depends on the χ-parameter [3,19]. It can have positive values, opposing mixing, zero for ideal mixtures, and negative values that encourage mixing. There may be different cases: if the components like each other more than themselves, we get $\chi < 0$, and if the components like themselves more than each other, we get $\chi > 0$ [3,19].

In Fig. 1.2, we illustrates schematic the phase diagram for a binary (AB) mixture [1]. Here, we consider attractive interactions between atoms of the same type (A-A and B-B) while there is repulsion between dissimilar A-B pairs. So, below the coexistence curve, the phase separation is energetically favorable. At $t = 0$, we quench the disordered system below the coexistence curve, leading to thermodynamic instability within the system. Consequently, A and B-rich domains begin to grow within the system.

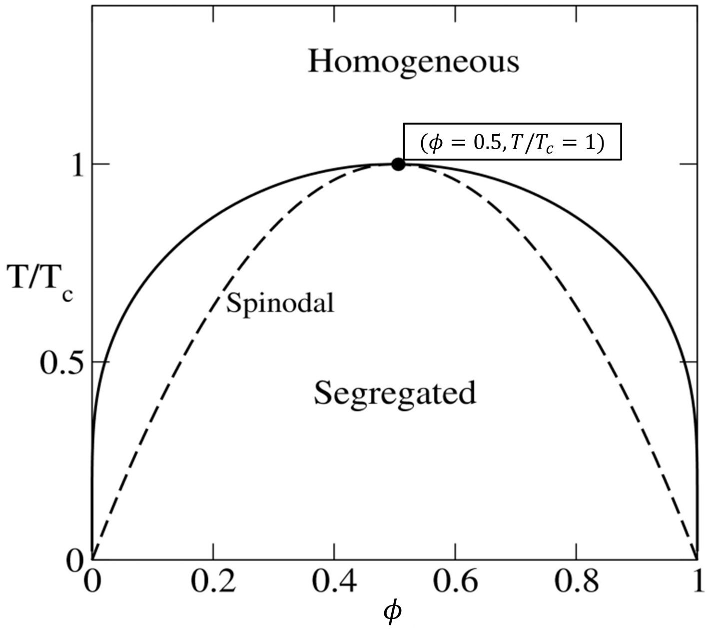

Fig. 1.2: Phase diagram for (AB) binary mixture [1]. ϕ depict the volume fraction and T represents the temperature. At the second-order critical point, $T/T_c = 1$, and $\phi = 0.5$. A solid line represents the coexistence curve. The system is in the homogeneously mixed state above the coexistence curve and starts the phase separating below it. The dashed line is a spinodal curve representing the metastable states between spinodal and coexistence curves.

The system follows the spinodal decomposition when we apply deep quench below the coexistence curve. During spinodal decomposition, even minor fluctuations in composition decrease free energy, driving spontaneous phase separation. When we quench the system near coexistence curve within the metastable regime, evolution occurs through the nucleation of droplets of the more stable phase. These droplets grow until they reach a size larger than some critical radius. Significant fluctuations are necessary within the metastable regime to generate domains larger than the critical size [3,19]. Let's calculate the energy required to nucleate the particle of size R. There will be a negative contribution to the free energy, which is proportional to the volume of the droplet. Initially, the system is globally unstable, and when it starts phase separation, the free energy reduces by ΔF_v per unit volume. Additionally, an interface is needed to create a droplet. Therefore, there is the positive contribution of interfacial energy γ, which is proportional to the surface area of the droplet. The change in free energy in nucleating the free droplet of size R, $\Delta F(R)$ is [3,19]:

$$\Delta F(R) = \frac{4}{3}\pi R^3 \Delta F_v + 4\pi R^2 \gamma. \tag{1.7}$$

For the critical size of the droplet, the free energy should be maximum. Therefore we can calculate the critical radius R^* of the droplet by differentiating above equation as [3,19]:

$$R^* = \frac{2\gamma}{\Delta F_v}. \tag{1.8}$$

We will discuss phase separation kinetics for simple fluids and polymeric mixtures in more detail later. In the following section, we discuss some basic characteristics of coarsening and growth of the domains.

1.2 Characterization of domain evolution and growth laws

When we quench the homogeneously mixed binary (AB) fluid below the critical temperature, corresponding domains evolve over time. The reduction in interfacial energy leads to the domain coarsening of A and B-type clusters. Here, we describe some physical quantities that characterize domain evolution. We also review the temporal variation of domain growth within the asymptotic time limit. According to the scaling hypothesis, average domain size $R(t)$ is a crucial quantity that characterizes dynamic aspects of the structure growth.

1.2.1 Radial distribution function

Using the radial distribution function (RDF) plots, we can quantify the distribution of particles around a reference particle at any given time. To compute the RDF, $g_{AB}(r)$ [20], we select a reference particle (A) positioned at the origin. Then, we assess the local number density of another particle (B) by partitioning the surrounding space into spherical shells of an uniform width, as depicted in the schematic illustrated in Fig. 1.3(a). Using the following relation, we can determine $g_{AB}(r)$ as [20]:

$$g_{AB}(r) = \frac{\rho_{AB}(r)}{\rho_B} = \frac{n_{AB}(r)/V_{shell}(r)}{N_B/V_{sim}} = \frac{V_{sim}}{V_{shell}(r)}\frac{1}{N_B}\left[\frac{1}{N_A}\sum_{i=1}^{N_A}\sum_{j=1}^{N_B}\delta(r-r_{ij})\right]. \qquad (1.9)$$

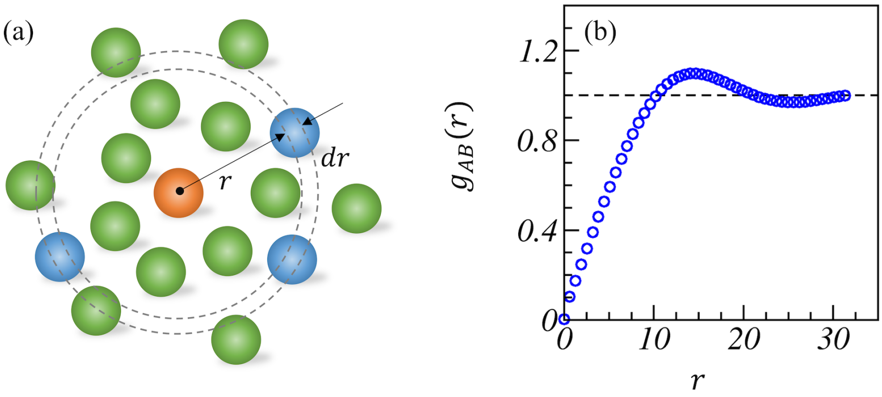

Fig. 1.3: (a) Schematic for calculating RDF at a distance r from the reference particle. (b) The general behavior of RDF representing the distribution of B-type particles around A in binary fluids.

In Eq.1.9, $\rho_{AB}(r)$ and ρ_B represents the local and total number density of B-type particles, respectively. These quantities can be formulated as $\rho_{AB}(r) = n_{AB}(r)/V_{shell}(r)$, and $\rho_B = N_B/V_{sim}$. Here, n_{AB} is the number of B-type particles in each bin around the reference particle A, $V_{shell}(r)$ and V_{sim} are the volume of each spherical shell and the volume of simulation box, respectively. N_A and N_B represents the total number of A and B-type particles in the system, respectively.

We have depicted the general behavior of RDF in Fig. 1.3(b) for a binary mixture. Typical to any fluid system, the RDF curve increases with distance and obtains a primary peak at a certain distance r representing the average separation between A and B type clusters. The formation of B-type cluster around A-type reference particle in other words. The position and height of the RDF peaks estimates the average distance between particles and system's spatial organization.

1.2.2 Local number density distribution

We calculate $\rho_A(x, y, z)$ to plot the density variation along a given direction ($x/y/z/$diagonal). For example, to calculate the local number density along x-direction at a fixed yz-plane), we use the equation [21,22]: $\rho_A(x, y, z) = n_A(x)/V_x$. Here, $n_A(x) = \sum_i \delta(x - r_i \cdot \hat{x})$, which denotes the number of A-type beads in the i^{th} slab of thickness $\Delta = 1.0$ on the yz plane located at position x. Additionally, $V_x = L^2 \times \Delta$ represents the volume of the slab, with L being the simulation box length along the y and z directions.

1.2.3 Correlation function and the structure factor

To characterize the domain evolution, we estimate the two essential and experimentally relevant functions, the correlation function and structure factor [1,6]. The two-point equal-time spatial correlation function has the following mathematical form:

$$C(\vec{r}, t) = \langle \psi\left(\vec{r}_1, t\right) \psi\left(\vec{r}_2, t\right) \rangle - \langle \psi\left(\vec{r}_1, t\right) \rangle \langle \psi\left(\vec{r}_2, t\right) \rangle . \tag{1.10}$$

Where $\psi(\vec{r}, t)$ is the order parameter, and angular brackets represent the ensemble average independent of initial conditions and thermal fluctuations. The structure factor can be expressed as the Fourier transform of the correlation function:

$$S(\vec{k},t) = \int d\vec{r} \exp\left(i\vec{k}\cdot\vec{r}\right) C(\vec{r},t). \tag{1.11}$$

where $\vec{k}$ represents the scattering wave vector.

To characterize the order of phases below the critical temperature, we define the order parameter at a given position $\vec{r}$ and time t as follows [23,24]:

$$\psi(\vec{r},t) = \frac{n_A(\vec{r},t) - n_B(\vec{r},t)}{n_A(\vec{r},t) + n_B(\vec{r},t)}. \tag{1.12}$$

where $n_A(\vec{r},t)$ and $n_B(\vec{r},t)$ depict the local number densities of A and B beads, respectively. To compute it, we divide the cubic simulation box into discrete unit cubes, and count the number of A and B particles in each cube. Note that, for $n_A(\vec{r},t) > n_B(\vec{r},t)$, $0 \leq \psi(\vec{r},t) \leq 1$, and for $n_A(\vec{r},t) < n_B(\vec{r},t)$, $-1 \leq \psi(\vec{r},t) \leq 0$. For the case of $n_A(\vec{r},t) = n_B(\vec{r},t)$, we assign $\psi(\vec{r},t) \in (0,1)$ or $\psi(\vec{r},t) \in (0,-1)$ with equal probability [24].

To get an idea about the interfaces and observe an appropriate Porod's law in $C(\vec{r},t)$ and $S(\vec{k},t)$, we harden the order parameter such as: $\psi(\vec{r},t) = +1$ for $\psi(\vec{r},t) > 0$, and $\psi(\vec{r},t) = -1$ for $\psi(\vec{r},t) < 0$ [23,25]. In a pure binary AB mixture, the correlation function decays as: $C(r,t) \approx 1 - ar^{\eta}...$ for $r \to 0$. This is known as Porod's law in correlation function [26,27]. Here a is a constant factor, and η is the surface exponent. For the scattering off sharp interfaces in pure mixtures, $\eta = 1$. Thus the correlation decays linearly as: $C(r,t) \approx 1 - ar...$ for $r \to 0$. The Porod's law in the structure factor [26,27] is defined as: $S(k,t) \sim k^{-(d+\eta)}$, for $k \to \infty$, where, d is the system dimensionality. In our case of $3d$ system of pure binary simple fluid, $d = 3$ and $\eta = 1$, therefore $S(k,t) \sim k^{-4}$, for $k \to \infty$.

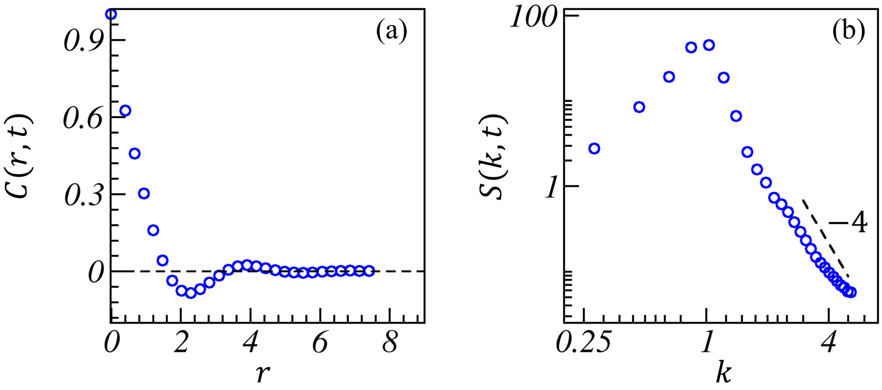

Fig. 1.4: Plots for the correlation function and corresponding structure factor curves for binary mixture are shown in (a) and (b), respectively. The black dashed line in (b) with a slope of -4 represents the Porod's tail in $3d$.

In the domain structure, only higher order Bragg reflections, occurring at $(2n+1)k_m$ where $n = 1, 2, 3, ...$, are visibly prominent. A narrow peak appears in the structure factor curve due to scattering around the most probable wave vector k_m. Physically significant wave vectors for a finite lattice are expressed as $k = (2n\pi/L)$, where $0 < n_i < L$ for $i = x, y, z$, and $n = (n_x, n_y, n_z)$ [25,28]. The oscillatory nature of the correlation function and number of peaks in $S(\vec{k}, t)$ (see Fig. 1.4) represent the ordering of evolved phases. We perform spherical averaging on these parameters for better statistical accuracy in analyzing the isotropic system. The corresponding scaled quantities are represented by $C(r,t)$ and $S(k,t)$, respectively [25,28].

1.2.4 Average domain length and growth laws

The average domain length can be calculated from the correlation function as a distance over which it decays to some fraction of its maximum value. It can also be defined as the inverse of the first moment of $S(k,t)$. Several alternative definitions of $R(t)$ exist which are equivalant in the asymptotic limit. In our case, we select a distance of 0.2 to measure $R(t)$ from the correlation function [15,29].

The presence of singular $R(t)$ is the fundamental assumption of scaling. Mathematically, we can write the scaled correlation and structure factor as [1,6]:

$$C(r,t) = f(r/R(t)). \tag{1.13}$$

$$S(k,t) = R(t)^d g(kR(t)). \tag{1.14}$$

Here, $f(r/R(t))$ and $g(kR(t))$ are the scaling functions.

Consider the phase separation kinetics of binary fluids. In this case, the flow field enables advective transport of the segregating components. The appropriate equation for the order parameter can be written as [1,6,30]

$$\frac{\delta\psi}{\delta t} + \vec{v}.\vec{\nabla}\psi = D\nabla^2\mu. \tag{1.15}$$

Here, $\vec{v}(\vec{r},t)$ is the fluid velocity field, D is the diffusion coefficient, μ is the chemical potential, and ψ is the order parameter. We consider that the fluid is incompressible. Therefore, the density, ρ, obeys the continuity equation:

$$\frac{\delta\rho}{\delta t} + \vec{\nabla}(\rho\vec{v}) = 0. \tag{1.16}$$

For an incompressible fluid, ρ is constant and $\vec{\nabla}.\vec{v} = 0$. The corresponding equation for the velocity field is the Navier–Stokes equation [1,6]:

$$\rho\left(\frac{\delta\vec{v}}{\delta t} + (\vec{v}\cdot\vec{\nabla})\vec{v}\right) = \eta\nabla^2\vec{v} - \vec{\nabla}p - \psi\vec{\nabla}\mu. \tag{1.17}$$

Here, p is the pressure, and η represents the fluid viscosity. The last term in Eq. 1.17 describes the force exerted on the fluid by the segregating mixture. Relevant to most experimental systems, the dynamics of the velocity field are much faster than those of the order-parameter field. Thus, the left-hand side of Eq. 1.17 can be set to zero. Moreover, the solution of the velocity in Fourier space [1,6]:

$$v_\alpha(\vec{k},t) = T_{\alpha\beta}(\vec{k})F_\beta(\vec{k},t). \tag{1.18}$$

$$T_{\alpha\beta}(\vec{k}) = \frac{1}{\eta k^2}\left(\delta_{\alpha\beta} - \frac{k_\alpha k_\beta}{k^2}\right). \tag{1.19}$$

$T_{\alpha\beta}(k)$ represents the Oseen tensor in Fourier space. In $d = 3$, Oseen tensor in real space can be expressed as:

$$T_{\alpha\beta}(\vec{r}) = \frac{1}{8\pi\eta r}\left(\delta_{\alpha\beta} + \frac{r_\alpha r_\beta}{r^2}\right). \tag{1.20}$$

As $\vec{\nabla}.\vec{v} = 0$, we can write the expresson for the order parameter:

$$\frac{\delta\psi}{\delta t} = D\nabla^2\mu - \int d\vec{r}'\left[\nabla\psi(r)\cdot T(\vec{r}-\vec{r}')\cdot\nabla'\psi(\vec{r}')\right]\mu(\vec{r}'). \tag{1.21}$$

This equation can be used to understand domain growth laws for coarsening in binary fluids. At early times, the growth is driven by diffusion, which crosses over to a hydrodynamic growth regime where the material is rapidly transported along domain boundaries by advection [31,32]. Let's estimate the different terms in Eq. 1.21. The left-hand side of the equation can be written as:

$$\frac{\delta\psi}{\delta t} = \frac{1}{R}\frac{dR(t)}{dt}. \tag{1.22}$$

Here, $R(t)$ is the domain length. At early times, the diffusive term can be estimated as $D\sigma/R^3$, where σ is the interfacial tension and $\mu = \sigma/R$. The advective term is of the order of $\sigma/\eta R$, where the Oseen tensor can be estimated as $T \sim 1/(\eta R)$ in $3d$. Thus the diffusive tern is dominant when: $D\sigma/R^3 \gg \sigma/\eta R$, or $R \ll (D\eta)^{1/2}$. In a diffusive regime, the growth can be written as:

$$\frac{\delta\psi}{\delta t} = \frac{1}{R}\frac{dR}{dt} \sim \frac{D\sigma}{R^3}. \tag{1.23}$$

$$R(t) \sim (D\sigma t)^{1/3}. \tag{1.24}$$

At later times, the advective term is dominant, and we can estimate the growth in this regime, the so-called viscous hydrodynamic regime:

$$\frac{1}{R}\frac{dR}{dt} \sim \frac{\sigma}{\eta R}. \tag{1.25}$$

$$R(t) \sim \sigma t/\eta. \tag{1.26}$$

At even later times, let's estimate the terms in Eq. 1.17. The fluid velocity can be estimated as R/t; therefore, the first tern of LHS is of the order of $\rho R/t^2$. The second term is of the same order. The viscous term in RHS is of the order of η/Rt, and the force term is σ/R^2. The terms on the LHS become comparable with those on the RHS at length scales of order $\eta^2/\rho\sigma$. Comparing the terms on both sides, we can get the growth law in an inertial hydrodynamic regime as:

$$\frac{\rho R}{t^2} \sim \frac{\sigma}{R^2}. \tag{1.27}$$

$$R(t) \sim (\sigma t^2/\rho)^{1/3}. \tag{1.28}$$

Typically for any physical system, $R(t)$ follows the general form of $R(t) = R_0 + at^{\phi}$. Here, R_0 represent the average domain size during the transient regime, occurring shortly after the quench at t_0, a is the constant that depends on temperature and composition [25,33–35]. For the critical compositions, the transient growth remains insignificant, whereas, in the case of off-critical mixtures, the evolution often starts with more pronounced transient growth regimes. Therefore, we redefine the domain growth law as, $R(t) \equiv R(t) - R_0$, and $t \equiv t - t_0$. Consequently, we can write $R(t) \sim t^{\phi}$ [1,6,33,35,36]. The growth exponent, ϕ, depends upon the coarsening mechanism and varies across three distinct growth regimes within macrophase separating systems [1,6,9,37,38]. These growth regimes are diffusive ($\phi \sim 1/3$), viscous hydrodynamic ($\phi \sim 1$), and inertial hydrodynamic ($\phi \sim 2/3$) for the $3d$ system [1,6]:

$$R(t) \sim \begin{cases} t^{1/3}, & R(t) \ll (D\eta)^{1/2} \\ t^{1}, & (D\eta)^{1/2} \ll R(t) \ll \eta^2/(\rho\sigma) \\ t^{2/3}, & R(t) \gg \eta^2/(\rho\sigma). \end{cases} \tag{1.29}$$

To estimate the appropriate value of ϕ, we graph $R(t)$ against t along a log-log scale [25,33–35]. Additionally, we adopt another intuitive approach to confirm this by computing ϕ_{eff} as:

$$\phi_{eff} = \frac{d \ln R(t)}{d \ln t} = \frac{\ln R(t_2) - \ln R(t_1)}{\ln t_2 - \ln t_1} \tag{1.30}$$

The higher time interval t_2 is integral multiple of t_1 as: $t_2 = \alpha t_1$. Therefore, we can write:

$$\phi_{eff} = \frac{\ln R(\alpha t_1)/R(t_1)}{\ln \alpha} \tag{1.31}$$

In general we can write the expression as:

$$\phi_{eff} = \log_\alpha \left[R\left(\alpha t\right) / R\left(t\right) \right]. \tag{1.32}$$

We plot ϕ_{eff} vs. $1/R(t)$ for the log-base $\alpha = 2$ [39].

In our study we have not taken care about the finite size effect. In both simulations and experimental studies, the system size is often limited due to computational or experimental costs. However, the behavior of the system in these confined conditions can differ significantly from its behavior in the bulk phase. This difference, known as the finite size effect, becomes particularly pronounced near phase transitions and critical points. Finite size effects result in deviations from the thermodynamic limit, affecting estimates of thermodynamic, structural, and transport properties, among others [40–42].

To mitigate these divergences, finite size scaling analysis can be applied. In this approach, we examine how physical quantities depend on system size. First, simulations are conducted for arange of system sizes, typically increasing in powers of two. For each system size, we calculate parameters such as the order parameter, specific heat, and susceptibility. By applying appropriate scaling laws, we then rescale and plot the data. Finally, we can extract critical exponents, such as ν, β, γ, and α, by analyzing these rescaled data.

1.3 General examples of phase separating systems

After briefly reviewing some important physical quantities useful for characterizing domain evolution, we focus on to a comparative study of the fundamental behavior exhibited by phase-separating binary (AB) simple fluid, polymer blend, and block copolymer melt systems using DPD simulation technique. Specifically, we analyze the results of domain evolution, characteristic functions, and growth laws. The schematic shown in Fig. 1.5 represents the fundamental structures of these three systems. To study the behavior of these systems in bulk, we have taken $3d$ box of size $64 \times 64 \times 64$ with number density, $\rho = 3$, where $A : B = 1 : 1$ (critical composition).

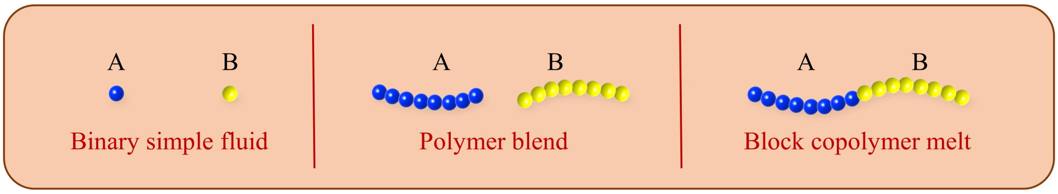

Fig. 1.5: Schematic represents the repeating units of simple fluids, polymer blends, and block copolymer melts.

1.3.1 Binary simple fluid

We consider a homogeneously mixed critical binary fluid and quenched the temperature of the system at $T = 1.0$ which is below the critical temperature T_c. After the quench, the system falls into the unstable state and spontaneously starts segregating into its constituents. In Fig. 1.6, we depict how the domains evolve over various time intervals after the quench. At $t = 0$, the initial homogeneous mixture is displayed in Fig. 1.6(a), which then undergoes segregation over time, as illustrated in Figs. 1.6(b)-1.6(e). Blue corresponds to the A-type beads, whereas yellow represents the B-type beads. Here, we have taken the reduced DPD units where time steps are measured in picoseconds, and length scales are in nanometers (we will discuss these concepts in the next section in more detail). To characterize the morphologies in Fig. 1.6(b)-1.6(e), we compute $g_{AB}(r)$ plotted against radial distance r in Fig. 1.6(f). The RDF peaks signify the ordering or clustering of domains within the system. Comparing the RDF curves corresponding to snapshots at different time steps, we observe that the prominent peaks shift towards higher r values. This indecates the formation of larger domains over time.

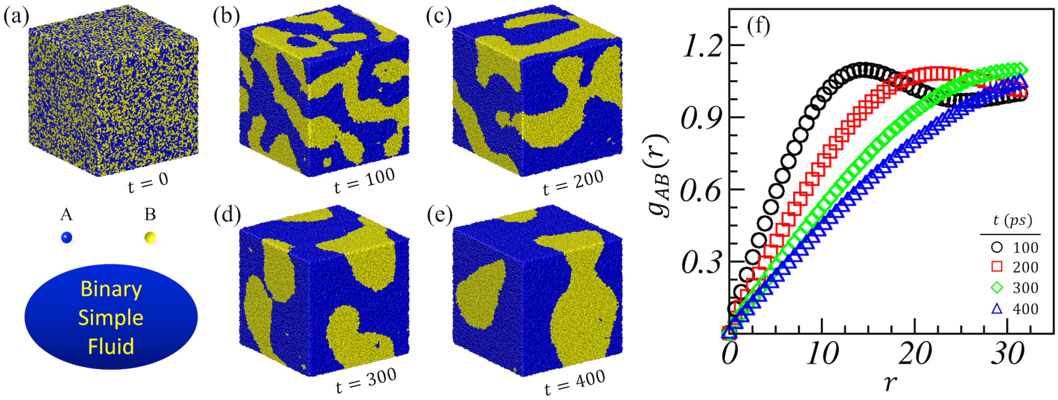

Fig. 1.6: (a-e) The evolution morphology of phase separating binary fluid at different time intervals, indicated alongside each image. (f) $g_{AB}(r)$ vs. r for different time intervals.

To characterize the phase evolution, we present the scaled correlation function, $C(r, t)$ vs. $r/R(t)$ in Fig. 1.7(a). The corresponding unscaled corrrelation is also shown in the inset. Zero crossing in the correlation function is plotted with a solid black line. As time progresses, the oscillatory nature of the correlation curves diminshes due to the formation of more significant cluster sizes. To comprehend this behavior, it is important to recall that the composition density is conserved in a binary fluid system with a boundary separating the two phases. The composition changes at the interface between the two phases, resulting in gradients in the order parameter, leading to the local density difference. The spatial correlation function measures the relationship between the density at two different points (say r_1 and r_2). Specifically, it quantifies the arrangement of components in the system. Due to the conservation constraint, the sum rule which only holds for compositionally symmetric system $\int C(\vec{r},t)d\vec{r} = 0$ is enforced, where $\vec{r} = \vec{r}_1 - \vec{r}_2$. As a result, the spatial correlation function oscillates when it encounters interfaces between the two phases. As the domains evolve, the number of interfaces reduces. Therefore, the oscillatory behavior of $C(r,t)$ diminishes with time. At much longer times, the domain size becomes comparable to the system size, resulting in the absence of oscillations of $C(r,t)$ around zero. Instead, the correlation function remains nonzero, indicating the presence of well-defined large domains consisting of the two components. After the scaling, we notice a good overlap in the correlation function, representing that the morphologies formed at different time intervals are statistically similar.

Further, we plot the scaled structure factor, $S(k,t)R(t)^{-3}$ vs. $kR(t)$ in Fig. 1.7(b) for different time intervals mentioned in the legends. Corresponding unscaled $S(k,t)$ vs. k is also shown in the inset. After scaling, a good overlap is noted in the structure factor data. Later, we notice the appearance of long tails in the structure factor having a slope of -4. This validates that the structure factor follows the Porod's law $S(k,t) \sim k^{-(d+1)}$, for $k \leftarrow \infty$, where $d = 3$ is the system's dimensionality. The occurence of Porod's tail results from the scattering off sharp interfaces.

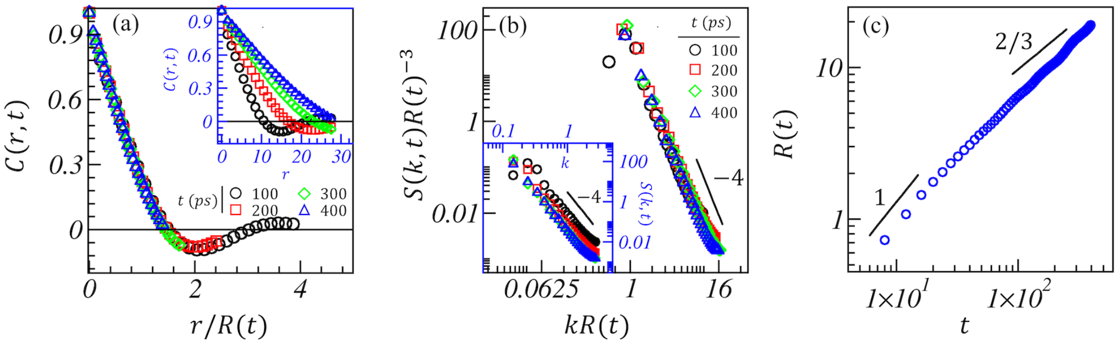

Fig. 1.7: (a) Plots for $C(r,t)$ vs. $r/R(t)$. (b) The structure factor $S(k,t)$ vs. $kR(t)$ at various time intervals, as indicated in the legends. The solid black line represents the porod's tail as $k \to \infty$. Inset of (a) and (b) plot the unscaled correlation and structure factor. (c) $R(t)$ vs. t for a simple fluid. Solid lines, characterized by slopes of 1 and 2/3, signify the phases of viscous and inertial hydrodynamic growth experienced by the system.

In Fig. 1.7(c), we plot the temporal variation of the characteristic length scale for a simple binary fluid mixture. The domain growth initially follows the viscous hydrodynamic growth ($\phi \sim 1$). Later, we notice a crossover to the inertial hydrodynamic regime with exponent $\phi \sim 2/3$. DPD is well-known for preserving the system's hydrodynamic behavior with a few hundred particles [43–46]. As a result, the system quickly transitions into the hydrodynamic regimes, rendering the early-time diffusive growth regime transient or short-lived. This behavior characterizes the macroscopic phase separation in binary fluids.

1.3.2 Binary polymer blend

Further, we are interested in the phase separation kinetics of polymer blend systems. We investigated a binary mixture comprising homopolymer chains containing A and B-type beads within a cubic box measuring $64 \times 64 \times 64$, with a density of 3. An equal number of particles (16 DPD beads) are considered in each polymer chain. We apply the temperature quench to the initial homogeneous polymer mixture at $T = 1.0$ below the critical temperatur T_c, which results in phase segregation. During the evolution, the previously discussed parameters are analyzed and compared over time. We illustrate the evolution snapshots in Figs. 1.8(a)-1.8(e) for different time intervals mentioned alongside them. (a) depict the initial homogeneous mixture at $t = 0$. After the quench, phase evolutions start within the system, forming phase-separated A and B-type clusters over time. The presence of bonded polymer chains results in slower phase segregations compared to the simple fluids (related snapshots shown in Fig 1.6(b)-1.6(e)). The corresponding RDF plots are shown in Fig. 1.8(f) for various time steps indicated in the legends. From the breadth of the prominent peaks, we can estimate the range of average domain sizes. The prominent peaks become broader and shift towards higher r values over time, indicating the formation of more evolved domains.

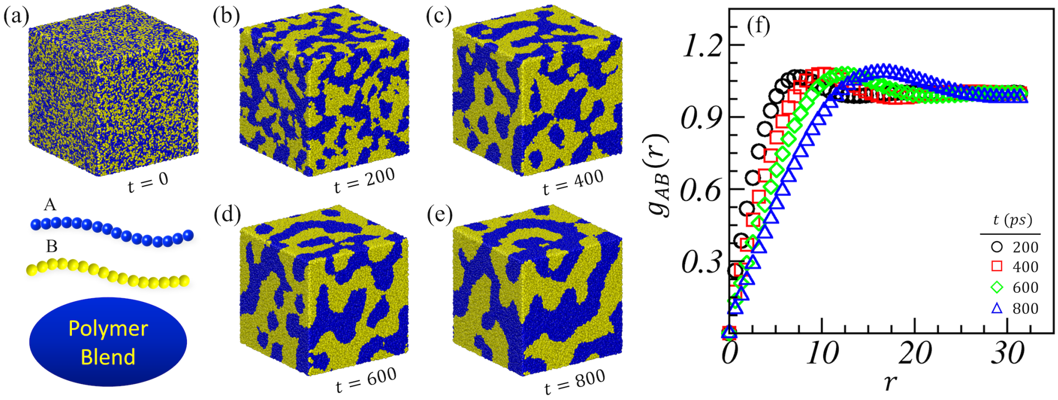

Fig. 1.8: We plot the evolved morphology of the polymer blend system in (a-e) at different time intervals. (f) plots the corresponding RDF curves.

Characteristic functions corresponding to the time evolution of the polymer blend system are depicted in Figs. 1.9(a) and 1.9(b). We notice the long tail in the black curve in $C(r, t)$ at the early time intervals, indicating the long-range correlation between microdomains. As time progresses, larger domains are formed, leading to the termination of $C(r, t)$ curves at smaller r values. Corresponding structure factor curves exhibit long tails at the late time, illustrating the phase-separated A and B clusters formed at later times. All curves follow Porod's law, signifying the sharp interfaces between the A and B-type domains. Inset of Figs. 1.9(a) and 1.9(b) represents the unscaled correlation and structure factor, respectively. After the scaling we notice the good overlap in $C(r,t)$, and $S(k,t)$, which represents the same statistical behavior

In Fig. 1.9(c), we plot $R(t)$ vs. time for polymer blend system. We observe a crossover from the early-time viscous hydrodynamic regime to inertial hydrodynamic growth. In polymer blend systems, the diffusive growth remains short-lived, resulting in macrophase separation, which leads to the formation of interconnected morphology.

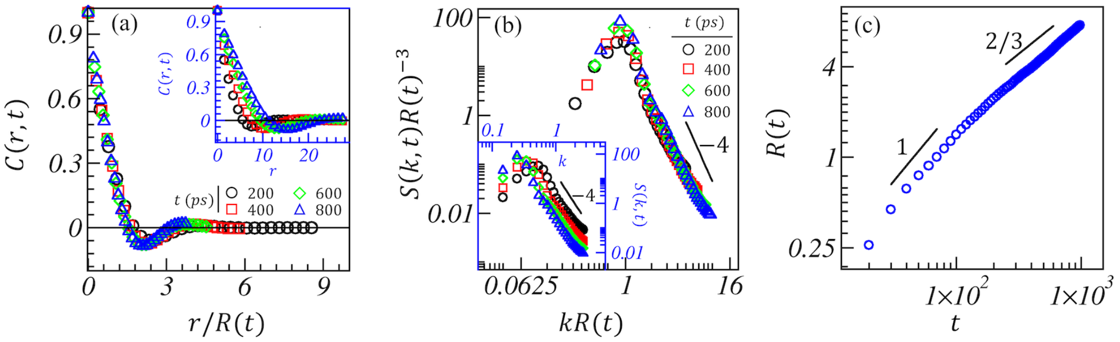

Fig. 1.9: In (a) and (b), we depict the scaled $C(r,t)$ vs. $r/R(t)$ and $S(k,t)$ vs. $kR(t)$, respectively, for different time intervals as indicated in the legends. Inset of (a) and (b) plot the unscaled correlation and structure factor. (c) The time-dependent behavior of $R(t)$.

1.3.3 Block copolymer melt

This section analyzes how block copolymer melts undergo phase separation over time. We have taken a cubic box with dimension $64 \times 64 \times 64$ with block copolymer chains composed of two blocks, A_nB_n, where each block consists of 8 DPD beads. The density is taken as $\rho = 3$. Initially, we start with a homogeneously mixed or uncorrelated state of the system. Subsequently, we quench the temperature of the system below its critical value and examine the evolution kinetics. In Figs. 1.10(a)-1.10(e), we depict the evolution snapshots at different time intervals. In the BCP chains, there is a bond constraint connecting two blocks, A and B. Consequently, after a specific time interval when the domain lengths are relatively equal to the average size of each block, frozen structures are observed. The corresponding RDF plots are depicted in Fig. 1.10(f). Periodic RDF peaks signify the microstructures formed in the system, with prominent peaks shifting towards higher r values, representing the evolved domains over time. The complete overlapping of the green and blue curves illustrates the frozen structures formed at t = 1800 and 2400, respectively.

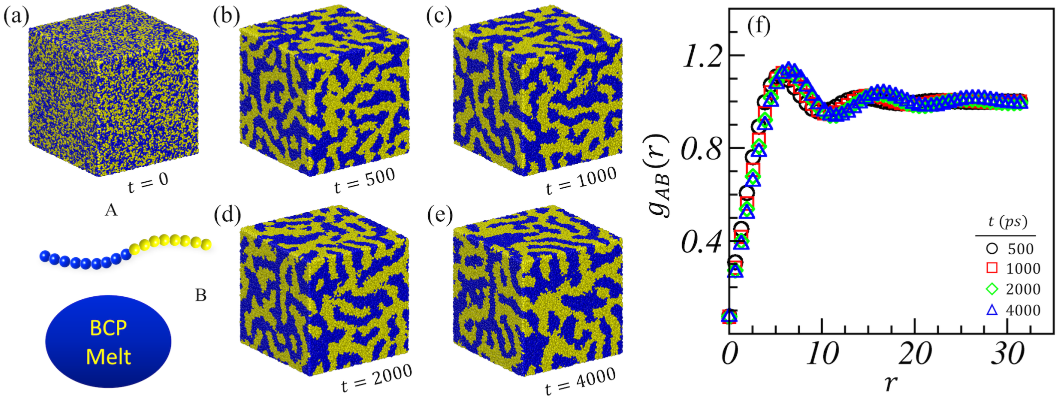

Fig. 1.10: In (a-e), snapshots of the domain morphology of the BCP melt system are shown at various time intervals. Corresponding RDF plots are depicted in (f).

The domain evolution is characterized by scaled correlation and structure factor plotted for different time intervals in Fig. 1.11. In Figs. 1.11(a) and 1.11(b), we have plotted the unscaled and scaled correlation function. The oscillatory peaks in $C(r,t)$ represent the formation of periodic microdomains in the system. As time progresses, the shift in the tails of the scaled correlation function at lower $r/R(t)$ values represents the formation of larger domains. In Figs. 1.11(c) and 1.11(d), we have plotted the unscaled and scaled structure factors, respectively, at different time intervals. The formation of periodic domains is evidenced by the appearance of a secondary hump in the structure factor curves. Frozen morphology is achieved in the BCP melt system at late time intervals. At each time interval, the tails of structure factor curves adhere to Porod's law. The good overlap in these data after the scaling represents the same class of universality followed by the system. It signifies that the morphology at different time steps is statistically similar.

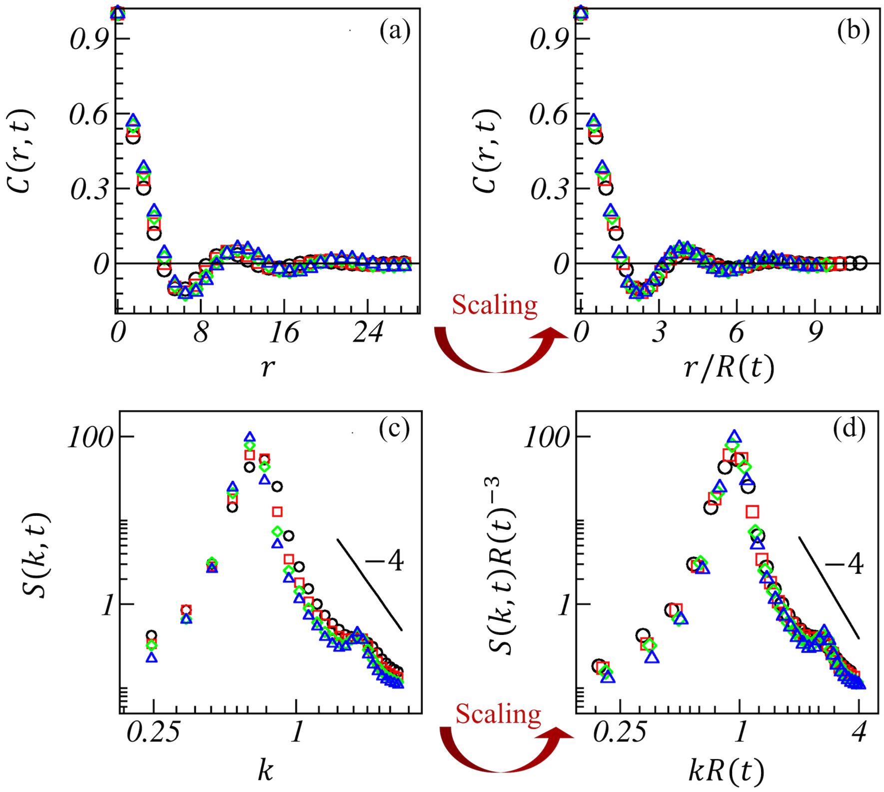

Fig. 1.11: In correspondence to the evolved morphology displayed in Fig. 1.10, we plot the unscaled and scaled correlation function in (a) and (b), respectively. (c) and (d) represent the unscaled and scaled structure factor.

The domain growth rate in the BCP melt system is notably slower compared to simple fluids and polymer blends. The characteristic length scale is plotted in Fig. 1.12 against time. The solid black line represents the diffusive growth followed by the system, which crosses over to saturation, forming frozen structures at the late time steps. The observed behavior represents the microphase separation occurring in BCP melt systems.

1.4 DPD simulation method

The DPD is very effective simulation technique used to model the kinetic properties of complex soft materials at mesoscale [43–45,47]. DPD simulation was first introduced by Hoogerbrugge and Koelman [46]. They developed the technique for the soft spheres,

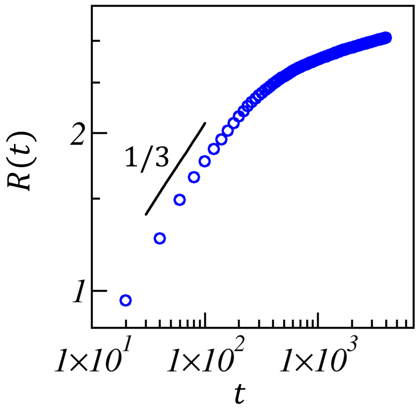

Fig. 1.12: Temporal variation of characteristic length scale $R(t)$ vs. t.

which later extended to polymers, surfactants, emulsions, biopolymers, liquids, and many other complex systems [43–45]. The technique was first formulated by Espanol et al. [45], with the study of fluctuation-dissipation theorem. We use the coarse graining in DPD method where a group of particles are considrered as a single DPD beads. This advantageous feature makes the DPD simulation more efficient to simulate it over a larger length and time scales compared to classical MD simulation [48–50].

The system dynamics is described by the Newton's equation of motion [43]:

$$\frac{d\vec{r}_i}{dt} = \vec{v}_i, \frac{d\vec{v}_i}{dt} = \vec{f}_i. \tag{1.33}$$

where $\vec{r}_i$ represents the position and $\vec{v}_i$ stands for the velocity of i^{th} bead. The mass of each particle is set to unity in reduced DPD units. The forces between the DPD beads have three components: (i) $\vec{F}_{ij}^C$, a conservative force arises due to the pairwise interaction between the particles, (ii) $\vec{F}_{ij}^D$, a dissipative force that tries to reduce the relative velocity between the particles, and (iii) $\vec{F}_{ij}^R$, a stochastic force which is the result of thermal fluctuations of the particles [44]. These forces are pairwise additive and can be written as:

$$\vec{f}_i = \sum_{i \neq j} \left[\vec{F}_{ij}^C + \vec{F}_{ij}^D + \vec{F}_{ij}^R \right]. \tag{1.34}$$

The preferable choice of $\vec{F}_{ij}^{C}$ is [43]:

$$\vec{F}_{ij}^{C} = \begin{cases} a_{ij}\left(1 - \frac{r_{ij}}{r_c}\right)\hat{r}_{ij}, & r_{ij} < r_c \\ 0, & r_{ij} \geq r_c. \end{cases} \tag{1.35}$$

were, a_{ij} represents the maximum repulsion between beads. $r_{ij} = |\vec{r}_{ij}|$ is the radial distance between the particles, $\hat{r}_{ij} = \vec{r}_{ij}/|\vec{r}_{ij}|$ is the force direction, r_c is the cut-off distance.

The forces $\vec{F}_{ij}^{D}$ and $\vec{F}_{ij}^{R}$ have the following functional forms [43]:

$$\vec{F}_{ij}^{D} = -\gamma\omega^{D}(r_{ij})(\hat{r}_{ij}.\vec{v}_{ij})\hat{r}_{ij}. \tag{1.36}$$

$$\vec{F}_{ij}^{R} = \sigma\omega^{R}(r_{ij})\Delta t^{-1/2}\xi_{ij}\hat{r}_{ij}. \tag{1.37}$$

Here, the strengths of these forces are given by γ and σ, respectively. $\vec{v}_{ij} = \vec{v}_i - \vec{v}_j$ represents the relative velocity between particles i and j. The direction of all three forces is along the line joining the center of interacting beads $\hat{r}_{ij}$. $\omega^{D}(r_{ij})$ and $\omega^{R}(r_{ij})$ depict the weight functions of $\vec{F}_{ij}^{D}$ and $\vec{F}_{ij}^{R}$, respectively. The parameter ξ_{ij} is the Gaussian distributed random number with zero mean and unit variance [43–45]:

$$\begin{aligned} \langle\xi_{ij}(t)\rangle &= 0, \\ \langle\xi_{ij}(t)\rangle &= (\delta_{ik}\delta_{jl} + \delta_{il}\delta_{jk})\delta(t - t'). \end{aligned} \tag{1.38}$$

Here, the symmetry property $\xi_{ij} = \xi_{ji}$ ensures the local momentum conservation throughout the system [43–45,47]. As we simulate the system at a constant temperature, the system must follow the fluctuation-dissipation theorem [44,45]:

$$\sigma^2 = 2\gamma k_B T. \tag{1.39}$$

The weight functions $\omega^D(r_{ij})$ and $\omega^R(r_{ij})$ have relation [43]:

$$\omega^D(r_{ij}) = \left[\omega^R(r_{ij})\right]^2 = \begin{cases} \left(1 - \frac{r_{ij}}{r_c}\right)^2, & r_{ij} < r_c \\ 0, & r_{ij} \geq r_c. \end{cases} \tag{1.40}$$

Here, T represents the equilibrium temperature of the system and k_B, the Boltzmann constant. However, other choices for the weight functions can also be considered as long as conditions in Eqs. (1.39) and (1.40) are satisfied [47]. The benefit of employing DPD simulation is that the three forces described in Eqs. 1.35-1.37 locally conserve momentum, ensuring accurate preservation of hydrodynamics of the complex fluids comprising only a few hundred particles [43,45].

1.4.1 Modeling polymer chains

We use the bead-spring model [51,52] to model the polymer chains. We consider the harmonic bond potential [51,52] to connect the polymer beads:

$$E_b = \frac{1}{2}k_b(r - r_0)^2. \tag{1.41}$$

Here, k_b is the elastic constant, and r_0 represents the equilibrium bond length. The angle potential can give the chain stiffness [51,52], defined as:

$$E_a = \frac{1}{2}k_a(\cos\theta - \cos\theta_0)^2. \tag{1.42}$$

Here, k_a and θ represent the strength of the angle potential and the angle between successive bonds along the chain with $\theta_0 = 180^\circ$. As we have taken soft potential in our simulation, there is a possibility of unphysical bond crossing between polymer chains. To overcome this, we adopted the *modified segmental repulsion potential (mSRP)* [53,54].

According to this potential, at the center of each bond, a pseudo-bead is considered, and the repulsive interaction is given between these pseudo beads (separated by the distance d_{ij}) [53]:

$$\vec{F}_{ij}^{mS} = k_{mS}\left(1 - d_{ij}/d_c^{mS}\right)\hat{d}_{ij}, \text{ for } d_{ij} < d_c^{mS}. \tag{1.43}$$

where k_{mS} is the force constant and d_c^{mS} is the cutoff distance for the mSRP interaction. $d_{ij} = |\vec{d}_{ij}|$ is the distance between pseudo beads, and $\hat{d}_{ij} = \vec{d}_{ij}/|\vec{d}_{ij}|$ is the direction of mSRP interaction.

1.4.2 Updates in position and velocity

Once we set the initial position (r_i) and velocity (v_i) of the constituent beads at a given time t, we integrate the Newton's equation of motion iteratively for subsequent time steps $t + \Delta t$. In DPD simulation, we employ the velocity-Verlet algorithm [43,48–50,55] to update the positions and velocities of beads. This involves a series of following updates executed sequentially over time:

$$r_i(t + \Delta t) = r_i(t) + v_i(t)\Delta t + \frac{1}{2} f_i(t)\Delta t^2 + O(\Delta t^3). \tag{1.44}$$

$$\bar{v}_i(t + \Delta t) = \bar{v}_i(t) + \frac{1}{2} f_i(t)\Delta t + O(\Delta t^2). \tag{1.45}$$

$$f_i(t + \Delta t) = f_i(r_i(t + \Delta t), \bar{v}_i(t + \Delta t)). \tag{1.46}$$

$$v_i(t + \Delta t) = \bar{v}_i(t + \Delta t) + \frac{1}{2} f_i(t + \Delta t)\Delta t + O(\Delta t^2). \tag{1.47}$$

In this prescribed sequence, we update the position based on the position (r_i), velocity (v_i) and force (f_i) from the previous time step. Following that, we perform the first velocity update to get updated interactions. Lastly, we update the particle velocities using the updated force and previously adjusted velocity.

1.4.3 Model parameters

In DPD simulation, the parameters r_c and k_BT serve as the characteristic length scale and energy scale of the system. We considered the equal mass of each DPD bead $m_i = m$. We have used the reduced DPD units for the simulation where we set the values of r_c, k_BT, and m equal to unity [43]. We have taken the density of system high as $\rho = 3$ [43]. We define the characteristic time scale as $\tau = \sqrt{(mr_c^2/k_BT)}$, and from the conventional DPD procedure, we get the simulation time step $\Delta t = 0.02\tau$ for the system integration. From the dimensional analysis, we get $\tau = 1$. We have chosen the value $\gamma = 4.5$ [56,57], which is particularly well-suited for the rapid equilibration and numerical stability of the system. We have chosen the value $\gamma = 4.5$ [56,57], which is particularly well-suited to maintain the balance between accurately capturing hydrodynamic behavior and keeping the computational efficiency of the system. At the given value of γ, the strength of the dissipative force is enough to mimic hydrodynamic interactions, and the system has numerical stability within the selected time steps [38,43].

We assume that a single DPD bead corresponds to ten water molecules. With the widely recognized properties of water molecules, each having a volume of 300 Å^3 for a mass density $1 gm/cm^3$ [58,59], we get that the characteristic length $r_c = 0.97\ nm$, and characteristic mass $m = 180\ Da$ [43,56–58,60]. Utilizing the characteristic length scale, mass, and energy k_BT at the room temperature, we can estimate that the characteristic time scale is $\tau = 8.3\ ps$ [43,58,61]. This denotes the inherent time scale for generating accelerated dynamics resulting from softcore potentials [43]. Yet, for a more pertinent time scale, we can correlate the collective diffusion coefficient of the polymeric melt in the DPD simulations, $D_{sim} \approx 1.74 \times 10^{-2}\ nm^2/\tau$, to the experimental time scales $D_{exp} \approx 2.00 \times 10^{-11}\ m^2/s$ [62]. Hence, we estimate the value $\tau \approx 0.87\ ns$.

Our simulation has coarse-grained ten water molecules in a single bead. Corresponding to the given situation, the repulsive interaction parameter between the same type beads

$(A-A$ and $B-B)$ is $a_{ij}=25$ (in units of k_BT/r_c) [43]. For the incompatible beads, the repulsive interaction is determined as $a_{ij}=a_{ii}+3.27\chi_{ij}$ [43], where χ_{ij} represents the Flory-Huggins interaction parameter between polymer beads. In this context, we have taken $\chi_{ij}\simeq 10.7$ (in reduced DPD unit), resulting in $a_{AB}=60$ [25,47,56,57,59,63].

We have taken the bond and angle potentials discussed earlier to model the flexible polymer chains. We used the optimized values of $r_0=0.5$, $k_b=64$, and $k_a=5$ [59,64,65]. To mitigate topology violations of polymer chains, we have utilized the mSRP potential with a strength of $k_S=100$ [53] and cutoff $d_c=0.8$ [53,66]. We subsequently observed that these parameter values facilitate phase separation in the polymeric system [25,47,63,64,67].

1.5 Overview of the thesis

Before going to the summary and discussion of this chapter, let's first provide an overview of each chapter in the thesis. In Chapter 2, we explore the effect of external light illumination on the kinetics of BCP melt systems. After the temperature quench, we apply the alternate on- and off-light cycles to the system with equal time intervals. We have considered the bonds joining the incompatible blocks of BCP chains to be photo-sensitive. During the on-cycle, the photo-sensitive bonds break with probability P_b, while the off-cycle results in bond recombination reactions of two active radicals with probability P_c. We observe that the system undergoes macrophase separation during on- and microphase separation during off-light cycles. The average domain length follows the power law growth, $R(t)\sim t^{\phi}$. The effective growth exponent ϕ demonstrates short-lived diffusive growth ($\phi\sim 1/3$) during the early stages. As time progresses, we notice a crossover from viscous ($\phi\sim 1$) to inertial ($\phi\sim 2/3$) hydrodynamic regime.

Next, we expanded our investigation to include the effect of random light illumination on polymeric fluids in Chapter 3. In this chapter, we have taken two scenarios: a polymer blend system where each polymer chain has an active radical at one end and a BCP melt system with photo-sensitive bonds between incompatible beads. First, we quench the initial homogeneously mixed system at a temperature below T_c. Simultaneously, we randomly apply light illumination to the system. Random photo-illumination leads to two stochastic events: (i) the breaking of photo-sensitive bonds and (ii) the bond recombination reaction of active radicals at polymer chains. At a fix P_c, we vary P_b, which mimics the variation in light intensity. $R(t)$ follows the power law behavior $R(t) \sim t^{\phi}$. As we increase P_b, both systems transition from micro-phase separation to macro-phase separation at specific transition probabilities. The chapter 2 and chapter 3 establish a solid framework for understanding the kinetics of polymer fluids, highlighting the influence of photo-sensitive bonds and active radicals.

In chapter 4, we study the impact of external shear on the BCP melt system. The BCP melt system is confined along z-direction with two rigid walls, one positioned at the top and another at the bottom. First, we quench the system below T_c and introduce velocity to the walls in a specific direction to induce shear within the system. We divided our study into four cases: (i) both walls remain stationary, (ii) the top wall moves in positive x-direction while the bottom wall is fixed, (iii) both walls are allowed to move in the same direction, and (iv) both walls move opposite in x-direction. We closely monitor how external shear influences various aspects, including the morphology, scaling function, growth laws, and other pertinent parameters. Domain growth exhibits the typical behavior observed in BCP melts, showing a cross-over from early-time diffusive growth to eventual saturation at late times. However, there is a significant change in the length scale when applying the shear. The key finding in this chapter is that shear accelerates the formation of a perfectly aligned lamellar structure along a specific direction much earlier than the usual BCP melt system.

In chapter 5, we extend our study of the BCP melt system, and explore the impact of external shear on the phase separation kinetics of critical and off-critical polymer blends. As discussed earlier, we again confined the system within amorphous solid walls and gave velocity to these walls along specific directions to apply shear on the system. First, we quench the system below T_c and apply an external shear following the different cases discussed earlier. In both systems, we observe the emergence of well-organized domains much earlier, particularly at high shear rates. The reorientation of domains occurs to overcome the external shear effect. The characteristic length scale represents a crossover from viscous ($\phi \sim 1$) to inertial ($\phi \sim 2/3$) hydrodynamic growth followed by the system. High shear rates lead to anisotropy development in the system, forming more stable structures. Comparatively, sustaining such structures in standard polymer blend systems is notably challenging. We noted the decrease in viscosity with increasing shear rate, representing the shear thinning for all cases. The study done in chapters 4 and 5 offers insights that could serve as a framework for predicting and designing anisotropic microstructures under the influence of external shear.

1.6 Summary and discussion

We have provided a broad overview of phase separation kinetics, illustrated by a simple example of magnetic system undergoing transition from a paramagnetic to a ferromagnetic state. Following that, we delved into the thermodynamics of mixing in binary fluid systems. We calculated the free energy of mixing and the Flory-Huggins interaction parameters. Depending on these relations, we discussed the corresponding phase diagram. Additionally, we provided a brief overview of spinodal decomposition and nucleation in phase-separating binary mixtures, highlighting their dependence on concentration ratio at $T < T_c$.

We discussed briefly the morphology and growth laws inherent in the kinetics of phase separation. The correlation function and the structure factor characterize domain morphology. The characteristic average domain size follows the power law behavior, $R(t) \sim t^{\phi}$, where ϕ exhibits three distinct growth regimes. We have provided an overview of the behavior of related parameters and extended our discussion to binary simple fluids, polymer blends, and block copolymer melt systems. We compared the domain evolution and growth laws in these systems to establish a reference for the systems investigated in the subsequent chapters.

In our work, we utilized the DPD simulation technique. The DPD method is a coarse grained simulation technique specifically designed to simulate complex systems. We employed specific potentials and forces to model polymer chains. Subsequently, we discussed the integration of the equation of motion and outlined the various parameter values utilized in the simulation.